nature sustainability

ARTICLES

https://doi.org/10.1038/s41893-021-00792-6

Check for updates

Bioinspired hierarchical porous membrane for efficient uranium extraction from seawater

Linsen Yang[1,2], Hongyan Xiao[1], Yongchao Qian[3], Xiaolu Zhao[1], Xiang-Yu Kong[1], Pei Liu[1,2], Weiwen Xin[1,2], Lin Fu[1,2], Lei Jiang[1,2] and Liping Wen[1,2] ✉

The oceans offer a virtually infinite source of uranium and could sustain nuclear power technology in terms of fuel supply. However, the current processes to extract uranium from seawater remain neither economically viable nor efficient enough to compete with uranium ore mining. Microporous polymers are emerging materials for the adsorption of uranyl ions due to their rich binding sites, but they still fall short of satisfactory performance. Here, inspired by the ubiquitous fractal structure in biology that is favourable for mass and fluid transfer, we describe a hierarchical porous membrane based on polymers of intrinsic microporosity that can capture uranium in seawater. This biomimetic membrane allows for rapid diffusion of uranium species, leading to a 20-fold higher uranium adsorption capacity in a uranium-spiked water solution (32 ppm) than the membrane with only intrinsic microporosity. Furthermore, in natural seawater, the membrane can extract as much uranium as 9.03 mg g^{-1} after four weeks. This work suggests a strategy to be extended to the rational design of a large family of microporous polymer adsorbents that could fulfil the vast promise of the oceans to fuel a reliable and potentially sustainable energy source.

Nuclear power is an important part of modern energy systems, and the demand for it is expected to double before 2040 (ref. [1]). Uranium is a key element in the nuclear industry[2,3]. In contrast to its limited availability on land (approximately 8 million tons of identified conventional resources)[4], the oceans contain more than 4.5 billion tons of uranium[5], representing an alternative and more abundant resource. However, the low uranium concentration (~3.3 μg l^{-1}) of seawater necessitates the use of high-selectivity, high-capacity sorbents[6]. Materials currently under development for effectively extracting uranium from natural water include highly porous materials with high specific surface area, including inorganic porous materials[7,8], metal–organic frameworks[9–11], covalent organic frameworks[12–14] and porous aromatic frameworks[11,15]. However, most of these sorbents are available in powder form and are thus unsuitable for actual use at scale. Hence, an increasing number of efforts have been made to develop self-standing, easily prepared and economical adsorbents.

Recent progress in the development of polymers of intrinsic microporosity (PIMs) allows for the design of sorbents with high specific surface areas that benefit from the highly rigid and contorted backbones of these polymers[16–18]. The high solubility of these polymers in common organic solvents makes it easy to prepare membranes of these materials[19]. These advantages indicate that PIMs and their functionalized derivatives have great potential for use in static adsorption applications, such as the recovery of uranium from seawater. Previous studies have attempted to use amidoxime-functionalized PIM-1 for the removal of uranyl ions from aqueous solution or seawater[20,21]. However, owing to the low capacity of the polymer and its large specific area, its high porosity cannot be maximally utilized during the adsorption process. Considering that some of the pores in PIMs are often subnanometre-sized[17], uranium adsorption on the membrane surfaces or fibres will invariably reduce the pore size, thus hampering uranium migration from the liquid phase into the sorbent. In this situation, mass transfer, and not the specific surface area or porosity, is the primary factor determining the adsorption capacity. Moreover, the resistance of mass transfer inside the microporous polymeric network has raised many concerns[22,23]. Supporting structures such as porous foam have been used to load the polymer, thus shortening the ion diffusion path[24]. However, despite the increased adsorption capacity, the introduced invalid mass of the foam and the low space utilization caused by massive macropores are still problems that need to be resolved. The internal structure of microporous sorbents therefore needs to be carefully designed.

Here, to ensure a high ion transfer rate and ready access to the adsorption sites in microporous membranes, we report a bioinspired, self-supporting amidoxime-functionalized polymer membrane with hierarchical porous structures for the efficient extraction of uranium from seawater. Fractal networks in organs such as blood vessels usually exhibit gradually decreasing diameters for branching and space-filling within a finite volume (Fig. 1a,b). This allows for mass transfer with high efficiency using only a small amount of energy[25–29]. Similarly, the artificial bionic membranes, which were fabricated by traditional non-solvent-induced phase separation (NIPS), contain high numbers of interconnected multiscale channels (Fig. 1c) and exhibit high permeability and reduced resistance to uranium migration. These channels coming from the exchange of solvent and non-solvent effectively divide the microporous polymer into smaller structural units suitable for mass transfer through micropores. Functionalization with amidoxime provides abundant active sites to bind the uranyl cations (Fig. 1d). Consequently, the uranium-adsorption capacity of the synthesized hierarchical porous membrane in a 32-ppm uranium-spiked solution is approximately 20 times that of the solution-cast membrane with intrinsic microporosity. The remarkable difference in the performances of the two membranes implies that the efficiency of mass transfer is the main factor determining the adsorption efficacy of microporous-membrane-based adsorbents. Furthermore,

[1]CAS Key Laboratory of Bio-inspired Materials and Interfacial Science, Technical Institute of Physics and Chemistry, Chinese Academy of Sciences, Beijing, P. R. China. [2]School of Future Technology, University of Chinese Academy of Sciences, Beijing, P. R. China. [3]Shaanxi Key Laboratory of Macromolecular Science and Technology, School of Chemistry and Chemical Engineering, Northwestern Polytechnical University, Xi'an, P. R. China. ✉e-mail: wen@mail.ipc.ac.cn

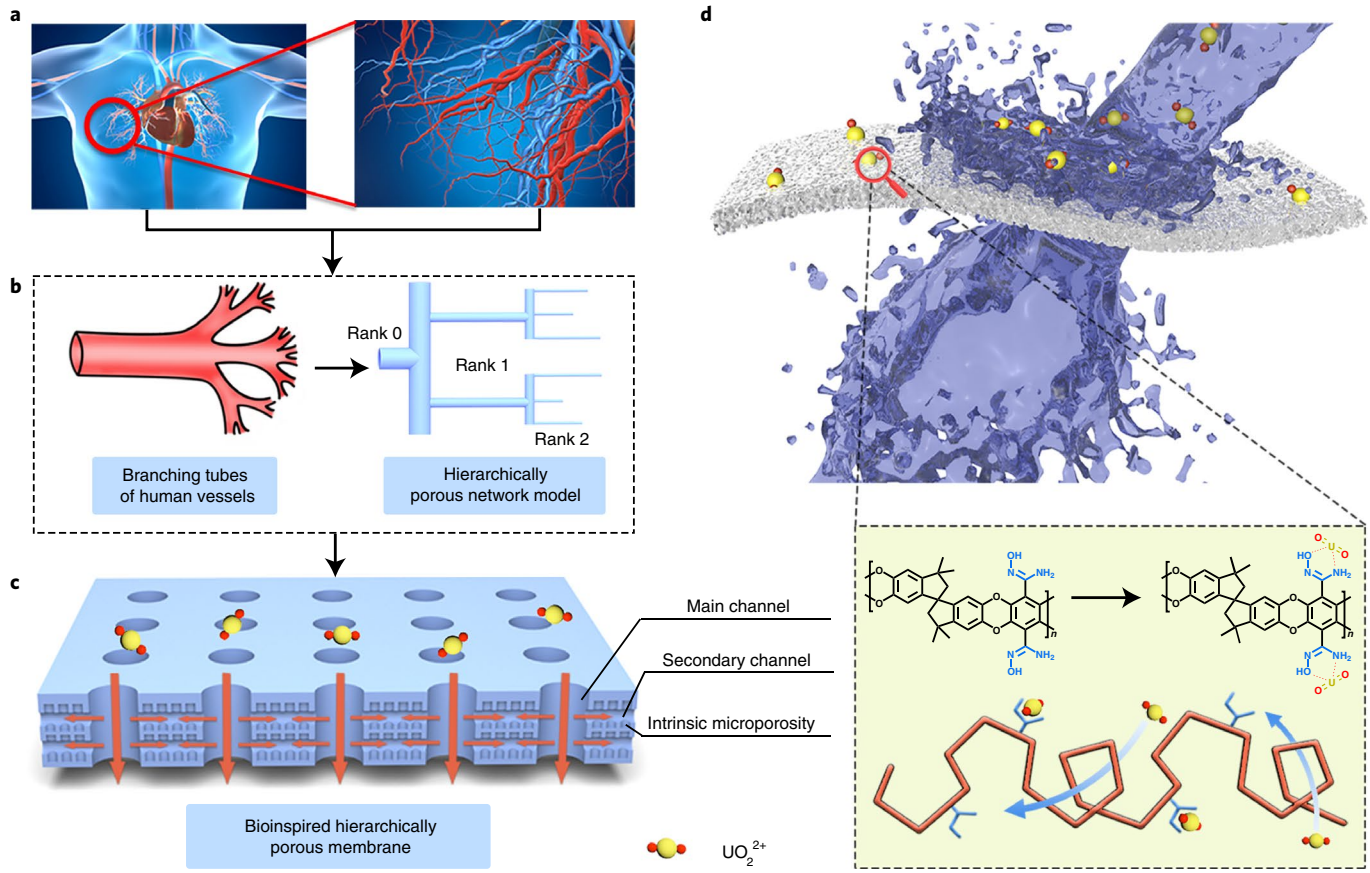

Fig. 1 | Biological inspiration and schematic of the bioinspired hierarchical porous membrane. a, Hierarchical networks of blood vessels in living organisms. **b**, Branched tube-based model inspired by the mammalian circulatory system. Increasing the number of branch points while reducing the branch diameter allows for efficient substance transfer at low energy consumption. **c**, Schematic illustration of the bioinspired hierarchical porous membrane. It contains pores with sizes on three different scales, including intrinsic micropores. **d**, Working principle of the hierarchical porous membrane for uranium adsorption. Amidoxime functionalization provides specific binding sites.

the membrane exhibits an uptake capacity of 9.03 mg g^{-1} after four weeks of adsorption in actual seawater, which is among the highest for membrane-based uranium extraction materials. Our work provides a universal method for enhancing the applicability of porous polymers as efficient membrane-based uranium sorbents.

Results

Synthesis and characterization. The synthesis of PIM-1 and PIM-1 with amidoxime groups (AO-PIM-1) is described in the Methods and Supplementary Fig. 1 (ref. [30]). The number-average molecular weight of PIM-1 was 1.27×10^5 g mol^{-1}, and the weight-average molecular weight was 3.51×10^5 g mol^{-1} (Supplementary Fig. 2). The Fourier transform infrared spectra of PIM-1 and AO-PIM-1 are shown in Fig. 2a. The disappearance of the nitrile peak (C≡N) at 2,240 cm^{-1} and the emergence of peaks at 1,655 cm^{-1} (C=N) and 915 cm^{-1} (N–O), which were related to the stretching vibrations of the amidoxime groups, confirmed the successful functionalization of PIM-1. The nuclear magnetic resonance spectrum of AO-PIM-1 (Fig. 2b) exhibits new peaks at 5.80 (–NH_2) and 9.45 (–OH) ppm. Thermogravimetric analysis was performed to investigate the thermal stabilities of powered PIM-1 and AO-PIM-1 samples (Supplementary Fig. 3). Compared with PIM-1, AO-PIM-1 underwent an additional step at approximately 200–300 °C before the degeneration of the backbone. This indicated the degradation of the amidoxime group. This result confirmed that the amidoxime groups are thermally stable in the conventional temperature range corresponding to uranium recovery[5].

Gas adsorption measurements were performed to determine the porosities of powdered PIM-1 and AO-PIM-1 samples. The previous studies that focused on gas separation or adsorption have tended to investigate the subnanometre structures of PIMs instead of their midsized micropores and mesopores, which are essential for liquid-phase mass transfer[31,32]. Hence, N_2 adsorption (at 77 K) was performed to estimate the Brunauer–Emmett–Teller surface areas of PIM-1 and AO-PIM-1, which were found to be 893 and 356 m^2 g^{-1}, respectively (Fig. 2c). A decrease in the Brunauer–Emmett–Teller surface area is generally attributable to tighter chain entanglement caused by the hydrogen bond interactions between the introduced amidoxime groups[17,20]. The quenched solid density functional theory method was employed to calculate the intraporosities of the materials. Functionalization with amidoxime decreased the pore volume from 0.650 to 0.318 cm^3 g^{-1}, which was still high. The tighter chains primarily reduced the size of the ultramicropores, instead of the micropores and mesopores. Consequently, the former did not come in contact with the N_2 gas during the measurements. The pore size distribution confirmed that the proportion of mesopores increased after the modification with amidoxime (Supplementary Fig. 4).

Fabrication of the hierarchical porous membrane. The hierarchical porous and self-supported AO-PIM-1 membrane was fabricated using NIPS. The membrane was characterized using scanning electron microscopy, which confirmed the presence of macropores with an approximate diameter of 20 μm running through the membrane (Fig. 2d). Smaller pores were distributed on the walls of the

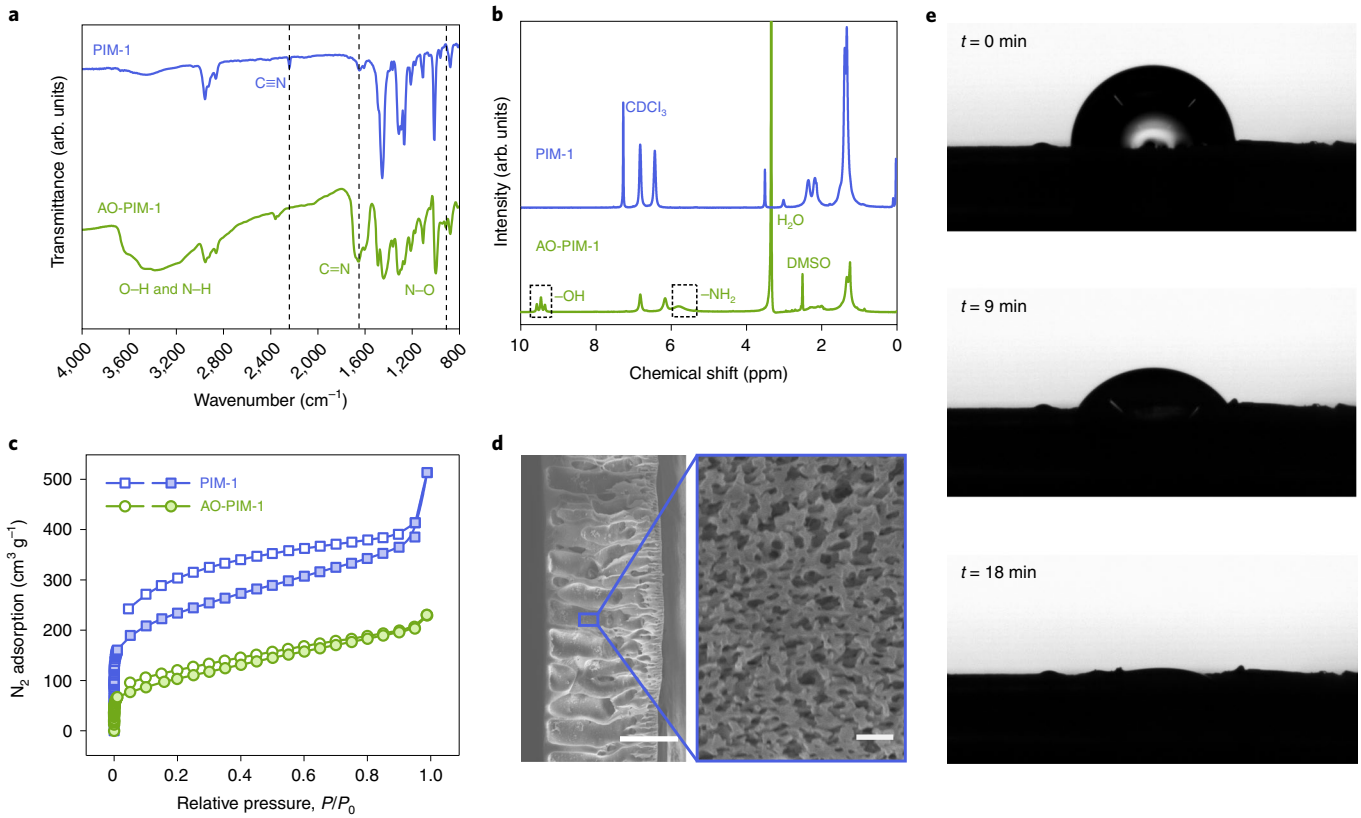

Fig. 2 | Characterization of PIM-1, AO-PIM-1 and the hierarchical porous membrane. a, Fourier transform infrared spectra of PIM-1 and AO-PIM-1. The disappearance of the nitrile peak and the appearance of new characteristic peaks related to amidoxime confirm the successful functionalization of PIM-1. **b**, Nuclear magnetic resonance spectra of PIM-1 and AO-PIM-1. New peaks related to hydroxyl and amino groups appeared after modification. $CDCl_3$, deuterated chloroform; DMSO, dimethyl sulfoxide-d6. **c**, N_2 adsorption/desorption isotherms of PIM-1 and AO-PIM-1 at 77 K. Hydrogen bonding interactions between amidoxime groups result in tighter stacking of polymer chains, thus reducing specific surface area. **d**, Scanning electron microscopy images showing a cross-section of the hierarchical porous membrane; nanoscale pores are present on the walls of through-membrane channels. Scale bars, 50 μm (left) and 1 μm (right). **e**, Wetting process of the compact layer. The compact layer took 18 min to change from the dry state to the superhydrophilic state, indicating that the thin and dense structure was highly permeable.

channels; these pores had sizes in the 300–500 nm range. This branched structure allowed uranium to be transferred into the membrane and transported throughout the system efficiently. The intrinsic pores existing in the nanonetworks could thus be maximally utilized. This phenomenon was similar to the transfer of substances along natural fractal structures. The formation of a characteristic compact layer is an inevitable consequence of NIPS. This top layer, which is generally too dense, invariably impedes mass transfer. In this study, we attempted to reduce the thickness of the compact layer as much as possible. As a result, this layer was far thinner than the rest of the membrane. The top view of the compact layer shows that it had a loose structure that was different from that of conventional NIPS membranes (Supplementary Fig. 5). Because the fabricated membrane was not used for regular purposes such as ion sieving or nanofiltration, these structural characteristics helped minimize the mass transfer resistance attributable to the dense layer, thus facilitating the rapid transport of uranium through the layer. The elemental analysis of the membrane was characterized by time-of-flight secondary ion mass spectrometry (ToF-SIMS). Combined with the reaction time and the characterizations, the conversion of cyano groups can be considered as 100% (ref. [17]). The nitrogen element therefore represents the distribution of amidoxime groups (Supplementary Fig. 6)[33,34]. We further investigated the wetting time of the top compact structure to estimate the permeability of the membrane. Figure 2f shows that the dense layer had a contact angle of 88.6° ± 0.2° initially, and after an 18-min spontaneous infiltration process, the dense layer became superhydrophilic due to the increase of water content. The short infiltration time indicates that the dense layer did not prevent the solution from fluxing through the membrane. Moreover, compared with adsorption processes that last days or even weeks, a short wetting time would make it easy for uranium to travel quickly through the body phase and into the sorbents used.

Adsorption performance with respect to uranium-spiked water samples. The uranium(VI) sorption performance of the hierarchical porous membrane was evaluated by immersing the membrane in 8-, 16- and 32-ppm uranium-spiked water samples (pH 5.5) for 50 h. The uranium concentrations of the solution were measured from their ultraviolet–visible absorption spectra. Arsenazo(III) was used as the chromogenic agent (Supplementary Fig. 7)[35]. The colour of the membrane changed from white to yellow after uranium adsorption (Fig. 3a). Adsorption was verified on the basis of the chemical composition of the uranium-loaded membrane, which was determined using X-ray photoelectron spectroscopy. Figure 3b shows the characteristic double peaks of U $4f_{5/2}$ (389.8 eV) and U $4f_{7/2}$ (378.7 eV) in the spectrum of the membrane after adsorption, in contrast to that before its use, which confirm the presence of uranium on the membrane surface. Further analyses were carried out on the basis of the high-resolution X-ray photoelectron spectroscopy U $4f_{5/2}$ and U $4f_{7/2}$ spectra, and the distribution of elemental uranium was mapped using energy-dispersive X-ray spectrometry (Supplementary Figs. 8 and 9).

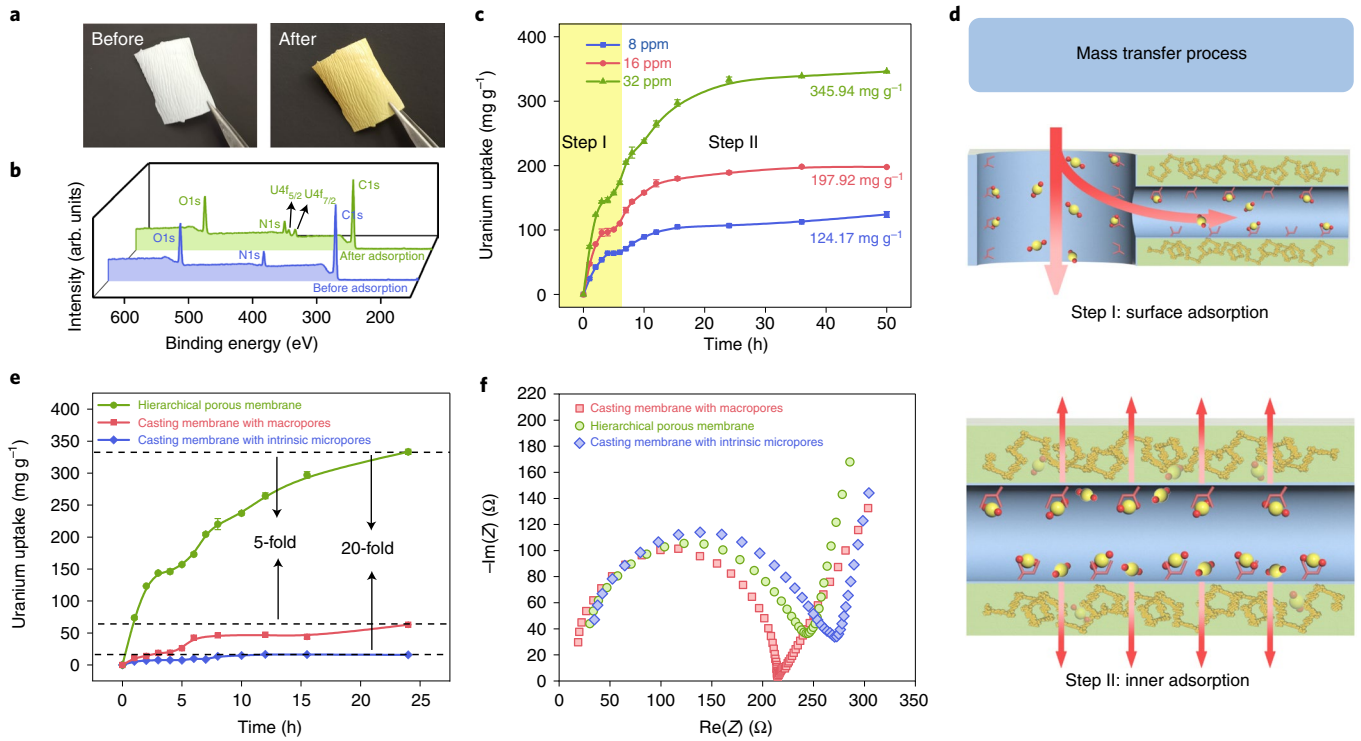

Fig. 3 | Uranium adsorption performance of the hierarchical porous membrane. a, Digital photographs of the membrane before and after uranium adsorption. **b**, X-ray photoelectron spectroscopy profile of membrane before and after uranium adsorption. The characteristic double peaks of uranium are located at 389.8 eV and 378.7 eV. **c**, Uranium adsorption capacities of the hierarchical porous membrane in uranium-spiked water with initial uranium concentrations of 8, 16 and 32 ppm. **d**, Mechanism of the two-step adsorption of uranyl ions by the hierarchical porous membrane. **e**, Uranium adsorption kinetics of the hierarchical porous NIPS membrane and two types of solution-cast control membrane in 32-ppm uranium-spiked solution. The capacity of the hierarchical porous membrane is about 20 times higher than that of the solution-cast membrane with intrinsic micropores, and about 5 times higher than that of the solution-cast membrane with macropores, which was made from a silicon template. **f**, Electrochemical impedance spectroscopy curves of the hierarchical porous NIPS membrane and two kinds of solution-cast control membrane in 0.3 M $UO_2(NO_3)_2$ solution. Z represents total impedance, Re(Z) is the real part of impedance and Im(Z) is the imaginary part of impedance. The error bars in **c** and **e** represent the standard deviation ($n=3$).

The adsorption kinetics were investigated to estimate the adsorption rate. After adsorption for 50 h (Fig. 3c), the saturated adsorption capacities of the membrane with respect to the 8-, 16- and 32-ppm solutions were 124.17, 197.92 and 345.94 mg g^{-1}, respectively. However, in contrast to the adsorption kinetics that depend on micropore diffusion, the hierarchical porous membrane exhibited two-step sorption behaviour. In the first step, adsorption plateaued in the initial 6 h because of the quick transfer of uranium from the bulk phase to the surfaces of the artificial macropores. In the second step, the uranyl ions diffused into the intrinsic micropores of the polymer (Fig. 3d). Uranium diffusion into the micropores would be slower than the external mass transfer process. The observed differences in the adsorption kinetics confirmed the advantages of using a membrane with biomimetic branching channels, as these allowed the ions to diffuse and fill the membrane quickly before being adsorbed in the micropores. In fact, this unique adsorption behaviour has been observed previously in a multiscale porous system based on particulate sorbents[36]. In the case of multiscale porous systems, the pores, whose sizes can span several scales, create an adsorption environment similar to that of intraparticle diffusion even if the sorbent is not particle-like in nature. Hence, the sorption processes were analysed using the Weber and Morris intraparticle diffusion model[37]. The linear fitting of the q_t–$t^{0.5}$ curves indicated that the curves consisted of three regimes with different slopes (Supplementary Fig. 10), suggesting that the mass transfer process is controlled by the following three steps: external surface transfer, surface-to-interior ion migration and intrapore diffusion.

The adsorption kinetics of the membrane were further evaluated using a pseudo-second-order kinetics model, and the correlation coefficients for the 8-, 16- and 32-ppm solutions were determined to be 0.9954, 0.9956 and 0.9933, respectively (Supplementary Fig. 11). The corresponding q_e and k_2 values were 133.16 mg g^{-1} and 2.49×10^{-5} g mg^{-1} min^{-1} for the 8-ppm solution, 218.34 mg g^{-1} and 1.80×10^{-5} g mg^{-1} min^{-1} for the 16-ppm solution, and 390.63 mg g^{-1} and 7.34×10^{-6} g mg^{-1} min^{-1} for the 32-ppm solution. The adsorption isotherm of the membrane was investigated using uranium-spiked water samples with concentrations of 4–150 ppm. The uranium uptake capacities could be fitted well using the Langmuir model, and the theoretical maximum adsorption capacity (q_m) was calculated to be 569.93 mg g^{-1} (Supplementary Fig. 12). The outstanding adsorption performance of the hierarchical porous membrane in aqueous solutions suggests that it is a competitive candidate for extracting uranium from actual seawater.

To explore the improved uranium adsorption capacity of the membrane, which depends on the introduced hierarchical pores, two solution-cast membranes with thicknesses similar to that of the compact layer of the NIPS membrane were prepared as controls. One such membrane (with a thickness of 7 µm; Supplementary Fig. 13) had intrinsic micropores, and another made from the silicon template (with a thickness of 8 µm; Supplementary Fig. 14) had 20 µm macropores and intrinsic micropores simultaneously. The solution-cast membrane with intrinsic micropores showed an unsatisfactorily low adsorption capacity of 15.66 mg g^{-1} in the 32-ppm solution (Fig. 3e). This value is 20 times lower than that of

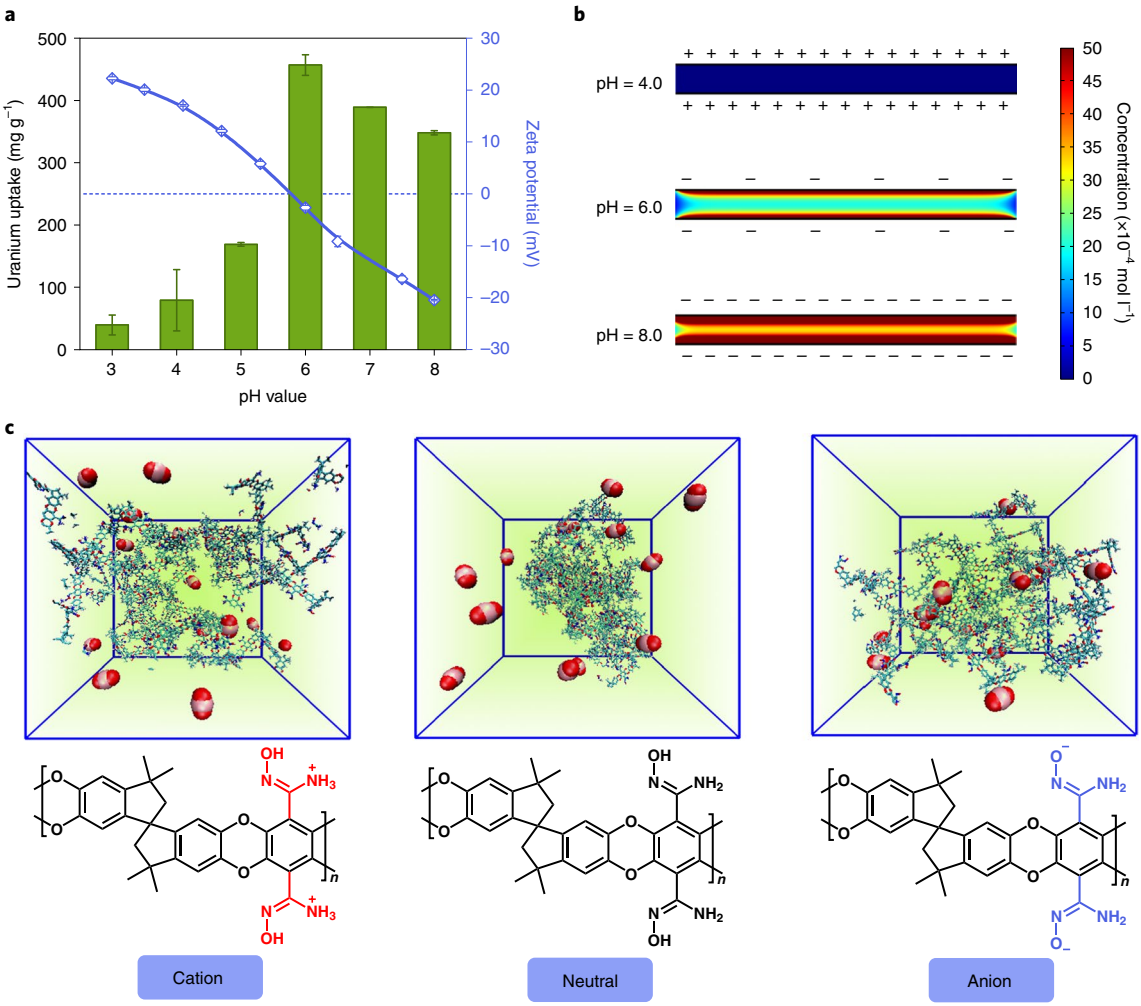

Fig. 4 | pH dependence of uranium adsorption performance of the hierarchical porous membrane. a, Effect of pH on uranium adsorption and zeta potential of the hierarchical porous membrane in 32-ppm uranium aqueous solution. The error bars represent the standard deviation ($n=3$). **b**, Results of the numerical simulations of uranyl diffusion in macropores at different pH levels. Uranyl cations tend to accumulate near the negatively charged surface. **c**, Results of the all-atom MD simulations of interactions between uranyl cations and the three AO-PIM-1 models (neutral, anion and cation) after equilibrium. The negatively charged backbone allows the uranyl cation to diffuse more easily into the intrinsic micropores.

the NIPS membrane. The solution-cast membrane with transmembrane macropores showed an adsorption capacity of 62.98 mg g^{-1}, which is five times lower than that of the NIPS membrane. The ionic conductivities of these three membranes were measured by electrochemical impedance spectroscopy to evaluate their ion transport behaviours. Figure 3f shows the Nyquist plots of the membranes in a 0.3 M $UO_2(NO_3)_2$ solution, and the equivalent circuit shown in Supplementary Fig. 15 was used to calculate the membrane resistance. The solution-cast membrane with macropores had the lowest resistance of 202.8 Ω due to transmembrane channels. However, the thicker NIPS membrane exhibited a lower resistance (208.7 Ω) than that of the solution-cast membrane containing intrinsic micropores (230.2 Ω). ToF-SIMS depth profiling was further used to explore the working mechanism of the hierarchical pores. Supplementary Fig. 16 shows the diffusion depth of uranium in micropores after the aforementioned solution-cast membrane adsorbed uranium for 24 h in a 32-ppm aqueous solution. The depth was approximately 200 nm, which is why the micrometre-thick solution-cast membranes showed insufficient adsorption capacities. In contrast, hierarchical channels allow for rapid ion transfer to the surface and regulate the microstructure near the intrinsic micropores, making it possible to fully exploit the high porosity of the membrane. It can therefore be concluded that the artificial fabrication of hierarchical structures in the AO-PIM-1 membrane efficiently improved the adsorption performance of the membrane.

pH dependence of uranium adsorption performance of the hierarchical porous membrane. The pH of the external environment is a key factor affecting the uranium adsorption performance of amidoxime-based sorbents. Uranium species in aqueous solution and natural seawater, which are controlled by pH values, have been studied before and were considered as an important factor influencing the adsorption capacity (Supplementary Fig. 17)[38–40]. Moreover, surface charge affects the diffusion and local concentration of uranium in micropores. As shown in Fig. 4a, when the pH value of the uranium-spiked solution (32 ppm) was lower than the surface isoelectric point, the repulsive forces between the positively charged surface and the uranyl cations and the protonation of the hydroxyl groups cooperatively reduced the adsorption capacity[41]. Once the membrane became negatively charged, its uranium uptake ability increased significantly. However, further alkaline enhancement would hydrolyse the uranyl cations and affect their existing form, thus reducing the adsorption capacity of the membrane. Finite element method and molecular dynamics (MD) simulations were performed to further

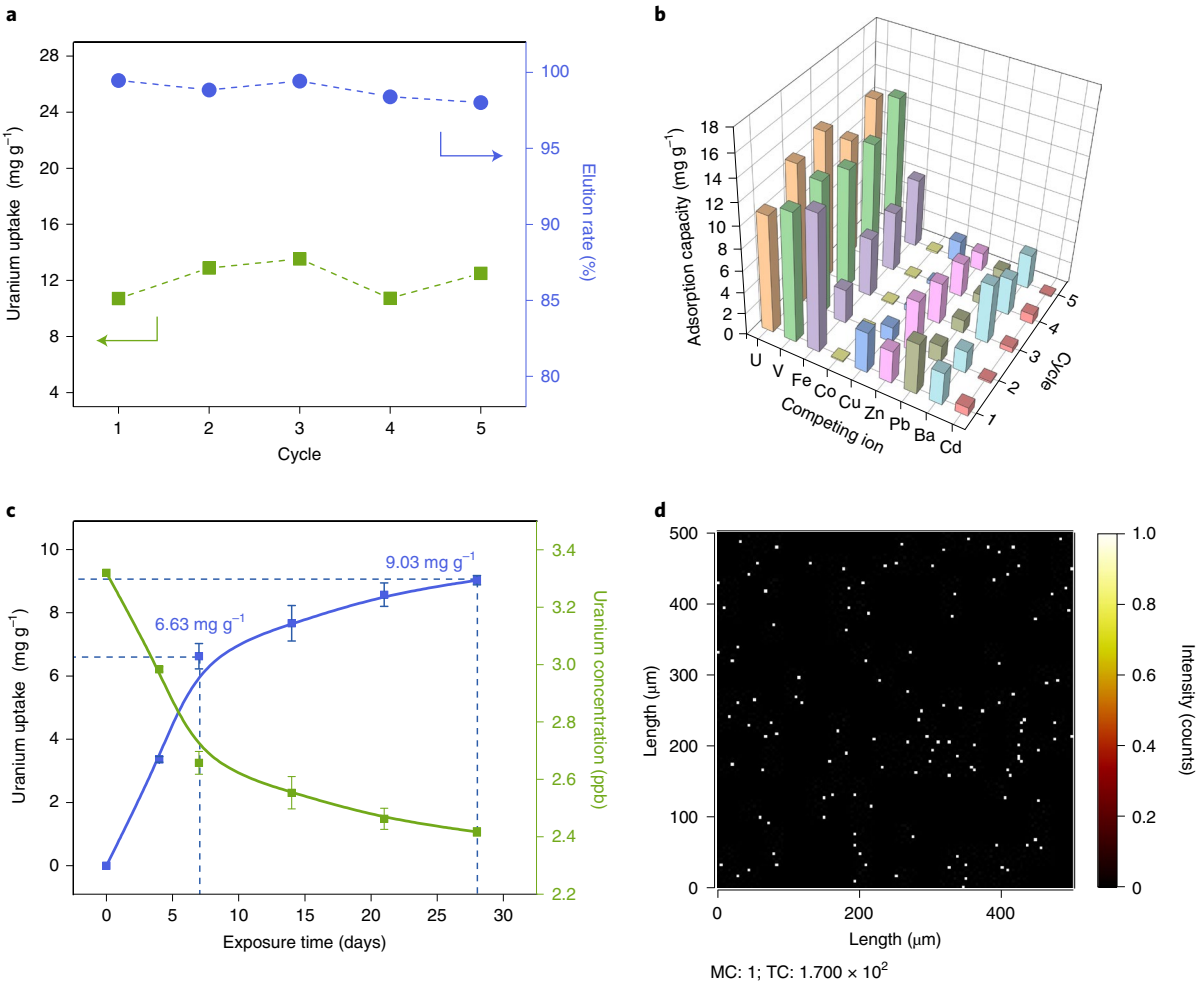

Fig. 5 | Reusability of the hierarchical porous membrane and its uranium adsorption performance in seawater. a, Uranium adsorption capacity and elution rate over five adsorption/desorption cycles in simulated seawater. **b**, Capacities of uranium and co-existing ions over five adsorption/desorption cycles in simulated seawater. **c**, Uranium extraction kinetics for 100 l of natural seawater over four weeks and variation in uranium concentration; the amount of sorbent used was 10 mg. The error bars represent the standard deviation ($n=3$). **d**, ToF-SIMS ion image of uranium on the hierarchical porous membrane after uranium extraction in natural seawater. MC represents the range of the colour scale and TC represents the total signal intensity (total counts).

analyse the surface-charge-controlled diffusion process and further explain the fluctuations in the adsorption capacity with the pH. Finite element method simulations based on the Poisson–Nernst–Planck theory are suitable for modelling branched macropores that are unaffected by the microscopic interactions between the molecular chains. Here, the macropores were considered to be one-dimensional nanochannels. Furthermore, the positively charged surface (pH 4.0) repulses the similarly charged uranyl ions, leading to a low concentration distribution within the nanochannels (Fig. 4b). When the surface charge becomes negative (pH 6.0), the ion concentration in the nanochannels increases, with the ions distributed mainly near the surface. An increase in the negative charge (pH 8.0) further promotes the diffusion of the uranyl ions, which then suffuse the entire nanochannel. These results confirmed that the surface charge controls the diffusion-based transport phenomenon, while the aggregation or dispersion of the uranyl ions near the secondary units affects their direct transfer within the micropores.

Figure 4c shows the interactions between the uranyl ions and the three AO-PIM-1 models, as determined through MD simulations of ion diffusion through the intrinsic micropores produced by the rigid molecular chain. The model of a single polymer chain included ten monomer units, and the terminal groups were capped with H atoms (Supplementary Fig. 18). In contrast to before equilibrium (Supplementary Fig. 19), uranyl ions are distributed more closely around the anionic AO-PIM-1 backbone after equilibrium, indicating that the interactions between the uranyl cations and the anionic AO-PIM-1 are stronger than those in the other two models. Compared with the other two models, the neutral model had the tightest chain stacking due to no electrostatic repulsion, hindering the ions from transferring close to the adsorption sites. Simultaneously, the electrostatic interaction energies between the uranyl cations and the anionic, neutral and cationic AO-PIM-1 were determined to be −8,560.7, −24.0 and 12.5 kJ mol^{-1}, respectively. The radial distribution functions for the O moiety of the OH group in AO-PIM-1 and the U moiety of the uranyl cation were also determined (Supplementary Fig. 20). The interactions between O and U in the anion model were the strongest among the three polymer models evaluated, and the distance between them was approximately 2.48 Å. The simulation results (including those of the structure, calculated electrostatic interaction energies and radial distribution functions) confirmed that the adsorption ability of the AO-PIM-1 membrane with respect to uranyl cations was the highest for the anion model, lower for the neutral model and the lowest for the cation model. These combined results confirmed that the membrane maintains a high adsorption capacity in a slightly alkaline environment. The pH of seawater usually fluctuates near 8.0,

which implies that the hierarchical porous membrane would exhibit optimal performance under natural conditions.

Reusability and selectivity of the hierarchical porous membrane for uranium adsorption. The reusability and selectivity of the hierarchical porous membrane were studied using adsorption/desorption experiments for five cycles in a simulated seawater system, which was prepared by adding extra co-existing ions to natural seawater (including U, V, Fe, Co, Cu, Zn, Pb, Ba and Cd; Supplementary Table 1). The uranium-loaded hierarchical porous membrane could be regenerated by immersion in an eluent (20 ml of 0.5 M HCl solution) for 1 h. As shown in Fig. 5a, the adsorption capacity of uranium remained stable and in the range of 10.71–13.54 mg g^{-1}. The elution rate of uranium was kept higher than 98%. The high reusability of the membrane indicates that it should be able to endure long periods of extraction, resulting in a decrease in the related economic cost. Moreover, during the five adsorption/desorption cycles, the adsorption capacities of other co-existing ions were also measured. Similar to other amidoxime sorbents, vanadium (10.99–13.24 mg g^{-1}) and iron (3.15–12.55 mg g^{-1}) were major competitive ions (Fig. 5b)[42–44]. The presence of co-existing interfering cations would reduce the uranium adsorption capacity. Furthermore, carbonate ions are also non-negligible because uranium usually exists as carbonate in natural seawater. The adsorbent therefore needs to compete with carbonate ions to adsorb the uranyl ions. According to a previous study, chemical reaction may be the rate-limiting step for uranium extraction in natural seawater[23]. The amount of each element that remained after elution was estimated from the ion concentration of the eluent (Supplementary Fig. 21). Compared with that of uranium, the elution of vanadium was more difficult during the desorption tests. Raising the eluant temperature and elution time may further reduce the residual rate, but the corresponding damage to the polymer chain should also be considered.

Uranium extraction from natural seawater using the hierarchical porous membrane. To confirm the ability of the hierarchical porous AO-PIM-1 membrane to extract uranium from natural seawater, a 10-mg membrane was placed between two pieces of sponge in a dialysis tube, and 100 l of natural seawater was continuously pumped through it (Supplementary Fig. 22). The membrane showed an adsorption capacity of 6.63 mg g^{-1} in the first week, which is higher than that mentioned in the Uranium Extraction from Seawater standard (6 mg g^{-1} in 21 days) (Fig. 5c)[11,15]. After 28 days of adsorption, the final concentration of uranium was reduced from 3.32 to 2.42 ppb, and the membrane achieved a uranium recovery capacity of approximately 9.03 ± 0.15 mg g^{-1}. The membrane was also digested in heated concentrated nitric acid to measure the adsorption capacity, which was 8.85 ± 0.09 mg g^{-1}. This high capacity places this membrane among the best-performing Uranium Extraction from Seawater materials reported so far (Supplementary Table 2). To further confirm the uranium extraction by the hierarchical porous membrane, the membrane surface was mapped using ToF-SIMS after the 28-day adsorption process in natural seawater. Figure 5d shows the ToF-SIMS ion image of uranium. This image clearly shows the uranium distribution, confirming the successful extraction of uranium by the hierarchical porous membrane. The signal had a scattered distribution and a low intensity compared with those of C, N and O due to the low concentration of uranium loaded on the membrane.

Discussion

Inspired by the high mass transfer efficiency of natural fractal networks, we prepared a hierarchical porous membrane based on amidoxime-functionalized PIM-1. The branched structure of the membrane helps avoid the restrictions on mass transfer caused by the decreases in pore size during adsorption in the subnanometre-sized pores. This allows the high specific surface area of the membrane to be maximally utilized. The adsorption capacity of the hierarchical porous membrane in a 32-ppm uranium-spiked solution was 20 times higher than that of a solution-cast membrane with only intrinsic micropores. Finite element method and MD simulations were performed to elucidate the effects of the surface charge and pH on the adsorption capacity. In natural seawater, the adsorption capacity of the membrane after one and four weeks was 6.63 mg g^{-1} and 9.03 mg g^{-1}, respectively. Considering the high performance of the membrane, it is a promising adsorbent for uranium extraction from seawater. Moreover, this method of forming hierarchical pores in membranes based on microporous polymers is ideal for reducing the mass transfer resistance of membranes.

Methods

Synthesis of PIM-1. Synthesis of PIM-1 powder was performed according to the published method[45]. 3,3,3′,3′-tetramethyl-1,1′-spirobisindane-5,5′,6,6′-tetrol (10.21 g, 30 mmol), 2,3,5,6-tetrafluoroterephthalonitrile (6.00 g, 30 mmol), anhydrous K_2CO_3 (8.40 g, 60.8 mmol), dimethylacetamide (200 ml) and toluene (100 ml) were added to a 500-ml three-necked round-bottom flask with a Dean–Stark trap, and the mixture was heated in an oil bath pre-heated to 160 °C for 1 h under N_2. When the reaction was stopped, the polymer was washed with water and methanol several times, and the solid was collected. The polymer was then dissolved in chloroform solution and re-precipitated by adding methanol for further purification. The bright-yellow product obtained after filtering was then dried at 110 °C for 12 h.

Synthesis of AO-PIM-1. Amidoxime functionalization was carried out following a reported procedure[20]. PIM-1 powder (1.8 g) was dissolved in tetrahydrofuran (120 ml) and heated to 69 °C. Hydroxylamine solution (14 ml, 50 wt% in H_2O) was added drop by drop, and the reaction was then refluxed for 23 h under N_2. The yellow solution was poured into ethanol (500 ml) after being cooled to room temperature, and the precipitated polymer was then washed by ethanol several times. The white product was dried at 100 °C for 12 h.

Membrane fabrication. AO-PIM-1 powder was dissolved in *N*,*N*-dimethylformamide to prepare a yellow solution with a concentration of 10 wt%. For the hierarchical porous membrane, the polymer solution was tape cast on a clean glass plate and immediately precipitated in a water bath (~50 °C). The white membranes were soaked in water for 12 h, and the water was replaced twice during this time. For the solution-cast membrane, the polymer solution was tape cast on a clean glass plate and then evaporated at room temperature overnight. The transparent membrane was dried in an oven at 100 °C for 24 h to remove the residual solvent. For the solution-cast membrane with macropores, 100 µl of the polymer solution was drop cast on a 2 cm × 2 cm silicon template with a column array. The column diameter was 20 µm, and the column spacing was 150 µm. The other operations were kept the same as for the solution-cast membrane.

Characterization. The Fourier transform infrared spectra were determined by a spectrometer (Varian Excalibur 3100) in transmittance mode. The nuclear magnetic resonance spectra were collected at room temperature using a Bruker Avance 400 spectrometer. The pore characteristics of the polymer powder were evaluated according to N_2 sorption isotherms at 77 K determined by a Quantachrome gas sorption analyser (Quadrasorb SI-MP). The thermal properties of the polymer were characterized by a Diamond TG-DTA6300 thermogravimetric analyser. The elemental analyses were determined by X-ray photoelectron spectroscopy (Thermo Scientific Escalab 250Xi) and ToF-SIMS (Ulvac-Phi PHI nanoToF II). The morphologies of the membranes were determined by scanning electron microscopy (SEM HITACHI S-4800). The water contact angle of the hierarchical porous membrane was measured using a Dataphysics water contact angle system (Dataphysics OCA50). The UV–Vis spectra were determined by a UV–Vis spectrophotometer (Shimadzu UV-2600). The concentration of uranium ions was determined using the inductively coupled plasma-mass spectrometer (ICP-MS; PerkinElmer NexION 300X). The surface zeta potential of the hierarchical porous membrane was measured by a zeta potential analyser (Anton Paar Surpass 3). The electrochemical workstation used was CHI660B.

Uranium adsorption in spiked water. To test the uranium adsorption capacity of the hierarchical porous membrane, 2 mg of the membrane was immersed in 200 ml of uranium-spiked deionized water and shaken for a fixed time. Each membrane was treated with 1 mM NaOH solution for 30 min at 60 °C before adsorption[42]. The pH of the solution in kinetics and isotherms was adjusted to 5.5 using NaOH solution. The concentrations of uranium in the solution were determined via UV–Vis absorption spectra on the basis of the specific peak at 652 nm for the complexation between Arsenazo(III) chromogenic agent and uranyl[35]. The uranium loaded on the membrane can be calculated using:

$$m_U = (C_0 - C_t) \times V \quad (1)$$

where m_U is the adsorption mass of uranium, C_0 is the original concentration of the solution, C_t is the concentration of uranium detected at a specific point t during the whole adsorption and V is the total volume of the solution. The pH values of the solutions were adjusted to 3.0, 4.0, 5.0, 6.0, 7.0 and 8.0 by using NaOH and HNO_3 solution.

Adsorption kinetics and isotherms. The adsorption data were analysed by the Weber and Morris intraparticle diffusion model based on:

$$q_t = k_{id} t^{0.5} \tag{2}$$

where q_t is the sorption capacity at time t (mg g^{-1}) and k_{id} is the rate constant of intraparticle diffusion.

The adsorption results were also analysed using the pseudo-second-order kinetics:

$$\frac{t}{q_t} = \frac{1}{(k_2 q_e^2)} + \frac{t}{q_e} \tag{3}$$

where q_e is the equilibrium adsorption capacity (mg g^{-1}), t is the time of adsorption (min) and k_2 is the adsorption rate constant (g mg^{-1} min^{-1}). The Langmuir equation shown below was also used to evaluate the uranium adsorption capacity of the membranes. The uranium uptake capacity of the hierarchical porous membrane was analysed by the Langmuir model:

$$\frac{C_e}{q_e} = \frac{1}{K_L q_m} + \frac{C_e}{q_m} \tag{4}$$

where C_e (ppm) is the concentration of uranium at equilibrium, q_m (mg g^{-1}) is the theoretical maximum adsorption capacity and K_L (1 mg^{-1}) is the Langmuir constant.

Determination of reusability and binding selectivity. Five consecutive adsorption/desorption cycles were performed to study the reusability and selectivity of the hierarchical porous membrane in simulated seawater. Nine metal ions were added to natural seawater (from the Yellow Sea, Tsingtao, China) to prepare the solution. The concentrations of U, V, Co, Cu, Zn, Pb and Cd were 100 times those in natural seawater. The concentrations of Fe and Ba were about 10 times higher than those in natural seawater (Supplementary Table 1). The pH value was adjusted to 8.0 ± 0.3 using NaOH. Subsequently, 5 mg of the hierarchical porous membrane was placed in 1 l of the above solution for 24 h at 25 °C. The adsorption capabilities for different ions were determined by ICP-MS. The ion-loaded membrane was then regenerated by immersion in an eluent (20 ml of 0.5 M HCl solution) with stirring at 25 °C for 1 h. After elution, the membrane was regenerated in an alkaline solution (20 ml of 5 mM NaOH) for 15 min and then used for the next cycle. The elution efficiency was calculated according to the concentration of ions in the eluent determined by ICP-MS.

Uranium adsorption in natural seawater. The above-mentioned natural seawater was used to estimate the uranium extraction capacity. The pH of the natural seawater was 8.09. The environment temperature was 27 °C. The seawater was filtered through filter membranes (0.2 μm) to remove the impurities and microorganisms before the experiments. Then, 10 mg of the hierarchical porous membrane was placed between two pieces of sponge in a continuous flowing-through system in which 100 l of seawater circularly flowed through a dialysis tube for four weeks. The flowing speed of seawater was controlled at about 2 l min^{-1}. The concentration of uranium and other competitive metal ions in natural seawater were measured by ICP-MS. The capacity was calculated by using:

$$q_t = \frac{(C_0 - C_t) \times V}{m} \tag{5}$$

where q_t (mg g^{-1}) is the capacity changing with the contact time, C_0 (ppb) is the initial uranium concentration in natural seawater (3.32 ppb), C_t (ppb) is the uranium concentration at time t, V (l) is the volume of seawater and m (g) is the weight of adsorbent.

The adsorption capacity was also verified by digesting the uranium-loaded membrane in 10 ml of heated concentrated nitric acid. The solution was diluted 1,000-fold using deionized water for analysis. The capacity was calculated using the following equation:

$$q_t = \frac{C \times V_d}{m} \tag{6}$$

where C (ppm) is the uranium concentration dissolved in concentrated nitric acid, V_d (l) is the volume of the acid and m (g) is the mass of the membrane.

Numerical simulation. Numerical simulation was performed using a commercial finite-element software package, COMSOL (version 4.2) Multiphysics. The Poisson–Nernst–Planck model is composed of a Poisson equation determining the electrostatic potential induced by moving ions and fixed charges, and a set of convection–diffusion equations representing the ion migration caused by the concentration gradient and electric field in the electrolyte solution, which is given as equations (7)–(9):

$$\nabla^2 \varphi = -\frac{F}{\varepsilon} \sum z_i c_i \tag{7}$$

$$j_i = D\left(\nabla c_i + \frac{z_i F c_i}{RT} \nabla \varphi\right) \tag{8}$$

$$\nabla \cdot j_i = 0 \tag{9}$$

where φ and ε are the electrical potential and dielectric constant of the solution, c_i is the ion concentration, z_i is the valence number, j_i is the ionic flux, D_i is the diffusion coefficient, R is the universal gas constant, T is the absolute temperature and F is the Faraday constant. The numerical simulated model was set as a rectangular channel with a length of 6,000 nm and a width of 500 nm. To reduce the mass transfer resistances at the entrance and exit of the channel, two electrolyte reservoirs were set. The ion flux at the boundaries had the zero normal components:

$$n \cdot j_i = 0 \tag{10}$$

where n is the unit normal vector to the wall surface.

The potential φ on the channel walls was calculated as:

$$n \cdot \nabla \varphi = -\frac{\sigma}{\varepsilon} \tag{11}$$

where σ is the surface charge density, which can be calculated through equations (12) and (13):

$$\sigma = \frac{\varepsilon \varepsilon_0 \xi}{\lambda_D} \tag{12}$$

$$\lambda_D = \sqrt{\frac{\varepsilon \varepsilon_0 RT}{2 n_{bulk} Z^2 F^2}} \tag{13}$$

where λ_D is the Debye length, ξ is the zeta potential of the membrane, ε is the permittivity of water, ε_0 is the permittivity of a vacuum, n_{bulk} is the solution concentration and Z is the valence number. The calculated values of σ at pH 4.0, 6.0 and 8.0 are 1.23×10^{-3} C m^{-2}, -1.96×10^{-4} C m^{-2} and -1.48×10^{-3} C m^{-2}, respectively.

MD simulations. MD simulations were performed on three polymer AO-PIM-1 models: the neutral, anion and cation types. A single polymer chain included ten monomer units, and the terminal groups were capped with H atoms as in the previous work[46]. Polymer amorphous models were constructed with ten polymer chains per simulation box. The initial simulation model was put into a cubic box (10.0 nm per side) with an initial density of about 0.0874 g cm^{-3}, and then the equilibration simulation referred to the 21-step compression/relaxation scheme by Larsen et al.[47]. Finally, the polymer AO-PIM-1 obtained was solvated in the solution box including 21,276 water molecules and 13 uranyl ions. Na^+ or Cl^- ions were added to make the solution neutral during the simulations. In this work, the uranyl concentration was set at 0.03 mol l^{-1} to reduce the simulation cost. The initial models were built using the Packmol package[48].

An all-atom OPLS-AA force field was then used with the GROMACS 2018.1 package in all the MD simulations[49–55]. The polymer chain topology file was done with the aid of GMXTOP[56]. The TIP3P water model was used. The partial charges for the neutral, anion and cation types of AO-PIM-1 monomers used the restrained electrostatic potential charges, which were obtained using the quantum mechanism calculation in the gas phase at the HF/6–31 G* level of theory using Gaussian 09 and fitted by the antechamber program using Ambertool[57,58]. The detailed simulation steps were as follows: (1) the initial model was energy-minimized to remove the system strain; (2) 200 ps NVT dynamics simulations were carried out, and the initial velocities were generated on the basis of a Maxwellian distribution at 300 K; (3) 2 ns equilibrium NPT dynamics simulations were carried out; and (4) the independent sampling analyses of 10 ns NPT MD simulations for each case were performed three times to obtain good statistics. All the covalent bond lengths were constrained by the LINCS algorithm, and a time step of 2.0 fs was used in all the simulations. The temperature was controlled using a velocity-rescaling thermostat with a relaxation time of 0.1 ps. The Berendsen pressure scaling was performed isotropically by coupling to a pressure bath of 10^5 Pa (with a time constant of 1.0 ps). The particle mesh Ewald summation method was used to calculate the electrostatic potential under periodic boundary conditions in all three spatial dimensions.

Data availability

The data that support the findings of this study are available in the paper and its Supplementary Information files.

Received: 10 February 2021; Accepted: 27 September 2021;
Published online: 29 November 2021

References

1. IEA *World Energy Outlook 2019* (OECD, 2019); https://doi.org/10.1787/caf32f3b-en
2. Chen, S., Xing, W. & Du, X. Forecast of the demand and supply plan of China's uranium resources till 2030. *Int. J. Green Energy* **14**, 638–649 (2017).
3. Chadwick, M. B. et al. ENDF/B-VII.0: next generation evaluated nuclear data library for nuclear science and technology. *Nucl. Data Sheets* **107**, 2931–3060 (2006).
4. *Uranium 2018: Resources, Production and Demand* (OECD Nuclear Energy Agency and the International Atomic Energy Agency, 2019); https://doi.org/10.1787/uranium-2018-en
5. Abney, C. W., Mayes, R. T., Saito, T. & Dai, S. Materials for the recovery of uranium from seawater. *Chem. Rev.* **117**, 13935–14013 (2017).
6. Ku, T.-L., Mathieu, G. G. & Knauss, K. G. Uranium in open ocean: concentration and isotopic composition. *Deep Sea Res.* **24**, 1005–1017 (1977).
7. Gunathilake, C., Górka, J., Dai, S. & Jaroniec, M. Amidoxime-modified mesoporous silica for uranium adsorption under seawater conditions. *J. Mater. Chem. A* **3**, 11650–11659 (2015).
8. Zhang, W., Ye, G. & Chen, J. Novel mesoporous silicas bearing phosphine oxide ligands with different alkyl chains for the binding of uranium in strong HNO_3 media. *J. Mater. Chem. A* **1**, 12706–12709 (2013).
9. Li, H. et al. Powerful uranium extraction strategy with combined ligand complexation and photocatalytic reduction by postsynthetically modified photoactive metal–organic frameworks. *Appl. Catal. B* **254**, 47–54 (2019).
10. Wang, L. L. et al. Ultrafast high-performance extraction of uranium from seawater without pretreatment using an acylamide- and carboxyl-functionalized metal–organic framework. *J. Mater. Chem. A* **3**, 13724–13730 (2015).
11. Yuan, Y. et al. A bio-inspired nano-pocket spatial structure for targeting uranyl capture. *Angew. Chem. Int. Ed.* **59**, 4262–4268 (2020).
12. Cui, W.-R. et al. Regenerable and stable sp^2 carbon-conjugated covalent organic frameworks for selective detection and extraction of uranium. *Nat. Commun.* **11**, 436 (2020).
13. Sun, Q. et al. Covalent organic frameworks as a decorating platform for utilization and affinity enhancement of chelating sites for radionuclide sequestration. *Adv. Mater.* **30**, 1705479 (2018).
14. Xiong, X. H. et al. Ammoniating covalent organic framework (COF) for high-performance and selective extraction of toxic and radioactive uranium ions. *Adv. Sci.* **6**, 1900547 (2019).
15. Li, Z. et al. Constructing amidoxime-modified porous adsorbents with open architecture for cost-effective and efficient uranium extraction. *Chem. Sci.* **11**, 4747–4752 (2020).
16. Li, C. et al. Engineered transport in microporous materials and membranes for clean energy technologies. *Adv. Mater.* **30**, 1704953 (2018).
17. Tan, R. et al. Hydrophilic microporous membranes for selective ion separation and flow-battery energy storage. *Nat. Mater.* **19**, 195–202 (2020).
18. Zuo, P. et al. Sulfonated microporous polymer membranes with fast and selective ion transport for electrochemical energy conversion and storage. *Angew. Chem. Int. Ed.* **59**, 9564–9573 (2020).
19. McKeown, N. B. Polymers of intrinsic microporosity (PIMs). *Polymer* **202**, 122736 (2020).
20. Satilmis, B., Isık, T., Demir, M. M. & Uyar, T. Amidoxime functionalized polymers of intrinsic microporosity (PIM-1) electrospun ultrafine fibers for rapid removal of uranyl ions from water. *Appl. Surf. Sci.* **467–468**, 648–657 (2019).
21. Sihn, Y. H., Byun, J., Patel, H. A., Lee, W. & Yavuz, C. T. Rapid extraction of uranium ions from seawater using novel porous polymeric adsorbents. *RSC Adv.* **6**, 45968–45976 (2016).
22. Dai, S. Catalyst: challenges in development of adsorbents for recovery of uranium from seawater. *Chem* **7**, 537–539 (2021).
23. Kim, J. et al. Characterization of uranium uptake kinetics from seawater in batch and flow-through experiments. *Ind. Eng. Chem. Res.* **52**, 9433–9440 (2013).
24. Dong, A. et al. Functionalization and fabrication of soluble polymers of intrinsic microporosity for CO_2 transformation and uranium extraction. *Eng. Sci.* **5**, 56–65 (2018).
25. McCulloh, K. A., Sperry, J. S. & Adler, F. R. Water transport in plants obeys Murray's law. *Nature* **421**, 939–942 (2003).
26. West, G. B., Brown, J. H. & Enquist, B. J. A general model for the origin of allometric scaling laws in biology. *Science* **276**, 122–126 (1997).
27. Sherman, T. F. On connecting large vessels to small: the meaning of Murray's law. *J. Gen. Physiol.* **78**, 431–453 (1981).
28. Wang, X. et al. Biomimetic fibrous Murray membranes with ultrafast water transport and evaporation for smart moisture-wicking fabrics. *ACS Nano* **13**, 1060–1070 (2019).
29. Zheng, X. et al. Bio-inspired Murray materials for mass transfer and activity. *Nat. Commun.* **8**, 14921 (2017).
30. Patel, H. A. & Yavuz, C. T. Noninvasive functionalization of polymers of intrinsic microporosity for enhanced CO_2 capture. *Chem. Commun.* **48**, 9989–9991 (2012).
31. Thompson, K. A. et al. *N*-Aryl-linked spirocyclic polymers for membrane separations of complex hydrocarbon mixtures. *Science* **369**, 310–315 (2020).
32. Yu, G. et al. Constructing connected paths between UiO-66 and PIM-1 to improve membrane CO_2 separation with crystal-like gas selectivity. *Adv. Mater.* **31**, 1806853 (2019).
33. Saito, T. et al. Uranium recovery from seawater: development of fiber adsorbents prepared via atom-transfer radical polymerization. *J. Mater. Chem. A* **2**, 14674–14681 (2014).
34. Wiechert, A. I. et al. Influence of hydrophilic groups and metal-ion adsorption on polymer-chain conformation of amidoxime-based uranium adsorbents. *J. Colloid Interface Sci.* **524**, 399–408 (2018).
35. Ma, C. et al. Sunlight polymerization of poly(amidoxime) hydrogel membrane for enhanced uranium extraction from seawater. *Adv. Sci.* **6**, 1900085 (2019).
36. Wang, X.-F. et al. Cooperative capture of uranyl ions by a carbonyl-bearing hierarchical-porous Cu–organic framework. *Angew. Chem. Int. Ed.* **58**, 18808–18812 (2019).
37. Weber, W. & Morris, J. C. Kinetics of adsorption on carbon from solution. *J. Sanit. Eng. Div.* **89**, 31–60 (1963).
38. Ladshaw, A. P. et al. First-principles integrated adsorption modeling for selective capture of uranium from seawater by polyamidoxime sorbent materials. *ACS Appl. Mater. Interfaces* **10**, 12580–12593 (2018).
39. Yuan, D. et al. Removal of uranium (VI) from aqueous solution by amidoxime functionalized superparamagnetic polymer microspheres prepared by a controlled radical polymerization in the presence of DPE. *Chem. Eng. J.* **285**, 358–367 (2016).
40. Endrizzi, F., Leggett, C. J. & Rao, L. Scientific basis for efficient extraction of uranium from seawater. I: Understanding the chemical speciation of uranium under seawater conditions. *Ind. Eng. Chem. Res.* **55**, 4249–4256 (2016).
41. Guo, X., Wang, Y., Li, C., Huai, P. & Wu, G. Optimum complexation of uranyl with amidoxime in aqueous solution under different pH levels: density functional theory calculations. *Mol. Phys.* **113**, 1327–1336 (2015).
42. Zhao, S. et al. A dual-surface amidoximated halloysite nanotube for high-efficiency economical uranium extraction from seawater. *Angew. Chem. Int. Ed.* **58**, 14979–14985 (2019).
43. Wiechert, A. I. et al. Uranium recovery from seawater using amidoxime-based braided polymers synthesized from acrylic fibers. *Ind. Eng. Chem. Res.* **59**, 13988–13996 (2020).
44. Xu, X. et al. Ultrahigh and economical uranium extraction from seawater via interconnected open-pore architecture poly(amidoxime) fiber. *J. Mater. Chem. A* **8**, 22032–22044 (2020).
45. Konnertz, N. et al. Molecular mobility of the high performance membrane polymer PIM-1 as investigated by dielectric spectroscopy. *ACS Macro Lett.* **5**, 528–532 (2016).
46. Heuchel, M., Fritsch, D., Budd, P. M., McKeown, N. B. & Hofmann, D. Atomistic packing model and free volume distribution of a polymer with intrinsic microporosity (PIM-1). *J. Membr. Sci.* **318**, 84–99 (2008).
47. Larsen, G. S., Lin, P., Hart, K. E. & Colina, C. M. Molecular simulations of PIM-1-like polymers of intrinsic microporosity. *Macromolecules* **44**, 6944–6951 (2011).
48. Martínez, L., Andrade, R., Birgin, E. G. & Martínez, J. M. PACKMOL: a package for building initial configurations for molecular dynamics simulations. *J. Comput. Chem.* **30**, 2157–2164 (2009).
49. Abraham, M. J. et al. GROMACS: high performance molecular simulations through multi-level parallelism from laptops to supercomputers. *SoftwareX* **1–2**, 19–25 (2015).
50. Berendsen, H. J. C., van der Spoel, D. & van Drunen, R. GROMACS: a message-passing parallel molecular dynamics implementation. *Comput. Phys. Commun.* **91**, 43–56 (1995).
51. Hess, B., Kutzner, C., van der Spoel, D. & Lindahl, E. GROMACS 4: algorithms for highly efficient, load-balanced, and scalable molecular simulation. *J. Chem. Theory Comput.* **4**, 435–447 (2008).
52. Lindahl, E., Hess, B. & van der Spoel, D. GROMACS 3.0: a package for molecular simulation and trajectory analysis. *J. Mol. Model.* **7**, 306–317 (2001).
53. Páll, S., Abraham, M. J., Kutzner, C., Hess, B. & Lindahl, E. in *Solving Software Challenges for Exascale* (eds Markidis, S. & Laure, E.) 3–27 (Lecture Notes in Computer Science 8759, Springer, 2015).
54. Pronk, S. et al. GROMACS 4.5: a high-throughput and highly parallel open source molecular simulation toolkit. *Bioinformatics* **29**, 845–854 (2013).
55. Van Der Spoel, D. et al. GROMACS: fast, flexible, and free. *J. Comput. Chem.* **26**, 1701–1718 (2005).
56. Larsen, G. S., Lin, P., Siperstein, F. R. & Colina, C. M. Methane adsorption in PIM-1. *Adsorption* **17**, 21–26 (2011).
57. *AMBER v.13* (Univ. California, San Francisco, 2013).

58. Frisch, M. et al. *Gaussian 09 Revision E.01* (Gaussian, 2009).

Acknowledgements
L.W. acknowledges funding support from the National Natural Science Foundation (grant no. 21625303) and the National Key R&D Program of China (grant nos 2017YFA0206904 and 2017YFA0206900). L.J. acknowledges funding support from the National Natural Science Foundation (grant no. 21988102). X.-Y.K. acknowledges funding support from the National Natural Science Foundation (grant no. 21905287).

Author contributions
L.W. proposed the research direction and guided the project. L.Y. designed and performed the experiments. L.Y., H.X., X.-Y.K., P.L., W.X., L.F. and L.J. analysed and discussed the experimental results and drafted the paper. H.X. performed the MD simulations. Y.Q. and X.Z. joined the discussion of the data and gave helpful suggestions. All authors contributed to the writing of the paper.

Competing interests
The authors declare no competing interests.

Additional information
Supplementary information The online version contains supplementary material available at https://doi.org/10.1038/s41893-021-00792-6.

Correspondence and requests for materials should be addressed to Liping Wen.

Peer review information *Nature Sustainability* thanks Chong Liu, Hongjuan Ma, Costas Tsouris and the other, anonymous, reviewer(s) for their contribution to the peer review of this work.

Reprints and permissions information is available at www.nature.com/reprints.

Publisher's note Springer Nature remains neutral with regard to jurisdictional claims in published maps and institutional affiliations.